J|A|C|S ARTICLES

Published on Web 09/08/2009

Dynamics of Reassembled Thioredoxin Studied by Magic Angle Spinning NMR: Snapshots from Different Time Scales

Jun Yang,[†,§] Maria Luisa Tasayco,[‡] and Tatyana Polenova*[,†]

Department of Chemistry and Biochemistry, University of Delaware, Newark, Delaware 19716, and Department of Chemistry, The City College of New York, Convent Avenue at 138th Street, New York, New York 10031

Received May 9, 2009; E-mail: tpolenov@mail.chem.udel.edu

Abstract: Solid-state NMR spectroscopy can be used to probe internal protein dynamics in the absence of the overall molecular tumbling. In this study, we report ^{15}N backbone dynamics in differentially enriched 1−73(U-^{13}C,^{15}N)/74−108(U-^{15}N) reassembled thioredoxin on multiple time scales using a series of 2D and 3D MAS NMR experiments probing the backbone amide ^{15}N longitudinal relaxation, ^{1}H−^{15}N dipolar order parameters, ^{15}N chemical shift anisotropy (CSA), and signal intensities in the temperature-dependent and ^{1}H T_2'-filtered NCA experiments. The spin-lattice relaxation rates R_1 ($R_1 = 1/T_1$) were observed in the range from 0.012 to 0.64 s^{-1}, indicating large site-to-site variations in dynamics on pico- to nanosecond time scales. The ^{1}H−^{15}N dipolar order parameters, $\langle S \rangle$, and ^{15}N CSA anisotropies, δ_σ, reveal the backbone mobilities in reassembled thioredoxin, as reflected in the average $\langle S \rangle = 0.89 \pm 0.06$ and $\delta_\sigma = 92.3 \pm 5.2$ ppm, respectively. From the aggregate of experimental data from different dynamics methods, some degree of correlation between the motions on the different time scales has been suggested. Analysis of the dynamics parameters derived from these solid-state NMR experiments indicates higher mobilities for the residues constituting irregular secondary structure elements than for those located in the α-helices and β-sheets, with no apparent systematic differences in dynamics between the α-helical and β-sheet residues. Remarkably, the dipolar order parameters derived from the solid-state NMR measurements and the corresponding solution NMR generalized order parameters display similar qualitative trends as a function of the residue number. The comparison of the solid-state dynamics parameters to the crystallographic B-factors has identified the contribution of static disorder to the B-factors. The combination of longitudinal relaxation, dipolar order parameter, and CSA line shape analyses employed in this study provides snapshots of dynamics and a new insight on the correlation of these motions on multiple time scales.

Introduction

Protein dynamics is essential for various biological functions, such as enzyme catalysis,[1−4] ion transport across biological membranes by ion channel proteins,[5−9] signaling,[10,11] and formation of misfolded proteins.[12−14] Internal motions in proteins range from small amplitude pico- to nanosecond scale movements to large conformational changes occurring on the time scales of microseconds to seconds. Characterization of dynamic behavior in proteins and protein assemblies on a wide range of time scales is necessary not only because insight may be gained into the functional significance of motions in a particular system but also because this knowledge may help establish general principles underlying dynamic properties of proteins as a function of the overall architecture and environment.

NMR is a powerful approach to study protein dynamics on multiple time scales from picoseconds to seconds.[15−27] Solid-state NMR methods can probe internal dynamics in the absence of the overall molecular tumbling, using anisotropic line shape analysis and relaxation measurements.[28−31] In solid-state NMR,

[†] University of Delaware.
[‡] The City College of New York.
[§] Current address: Institut für Biophysicalische Chemie, Goethe Universität, Max-von-Laue-Str. 9, Biozentrum N202, 60438 Frankfurt am Main, Germany.

(1) McDermott, A.; Polenova, T. *Curr. Opin. Struct. Biol.* **2007**, *17*, 617–622.
(2) Butterwick, J. A.; Palmer, A. G. *Protein Sci.* **2006**, *15*, 2697–2707.
(3) Loria, J. P.; Berlow, R. B.; Watt, E. D. *Acc. Chem. Res.* **2008**, *41*, 214–221.
(4) Kern, D. *Biochemistry* **2003**, *42*, 8605–8605.
(5) Baker, K. A.; Tzitzilonis, C.; Kwiatkowski, W.; Choe, S.; Riek, R. *Nat. Struct. Mol. Biol.* **2007**, *14*, 1089–1095.
(6) Varga, K.; Tian, L.; McDermott, A. E. *Biochim. Biophys. Acta, Proteins Proteomics* **2007**, *1774*, 1604–1613.
(7) Lange, A.; Giller, K.; Hornig, S.; Martin-Eauclaire, M. F.; Pongs, O.; Becker, S.; Baldus, M. *Nature* **2006**, *440*, 959–962.
(8) Ader, C.; Schneider, R.; Hornig, S.; Velisetty, P.; Wilson, E. M.; Lange, A.; Giller, K.; Ohmert, I.; Martin-Eauclaire, M. F.; Trauner, D.; Becker, S.; Pongs, O.; Baldus, M. *Nat. Struct. Mol. Biol.* **2008**, *15*, 605–612.
(9) Roux, B.; Allen, T.; Berneche, S.; Im, W. *Q. Rev. Biophys.* **2004**, *37*, 15–103.
(10) Tsao, D. H. H.; Hum, W. T.; Hsu, S.; Malakian, K.; Lin, L. L. *J. Biomol. NMR* **2007**, *39*, 337–342.
(11) Abdulaev, N. G.; Ramon, E.; Ngo, T.; Brabazon, D. M.; Marino, J. P.; Ridge, K. D. *FASEB J.* **2007**, *21*, A982–A983.
(12) Sprangers, R.; Kay, L. E. *Nature* **2007**, *445*, 618–622.
(13) Barducci, A.; Chelli, R.; Procacci, P.; Schettino, V.; Gervasio, F. L.; Parrinello, M. *J. Am. Chem. Soc.* **2006**, *128*, 2705–2710.
(14) Bollen, Y. J. M.; Kamphuis, M. B.; van Mierlo, C. P. M. *Proc. Natl. Acad. Sci. U.S.A.* **2006**, *103*, 4095–4100.
(15) Cole, H. B. R.; Torchia, D. A. *Chem. Phys.* **1991**, *158*, 271–281.
(16) Torchia, D. A. *Annu. Rev. Biophys. Bioeng.* **1984**, *13*, 125–144.

10.1021/ja9037802 CCC: $40.75

the anisotropic resonance frequency depends on the orientation of the molecular frame with respect to the static magnetic field. The motions with the correlation times faster than the inverse of the corresponding anisotropic interactions partially average the orientational dependence and thus decrease the width of the anisotropic spectra. These motionally narrowed spectra contain information about the amplitude and the correlation time of the motions. For example, the anisotropic ^{2}H line shapes determined by quadrupolar, dipolar, and chemical shift anisotropy (CSA) interactions were generally used to probe dynamics in peptides and proteins by solid-state NMR.[29,30,32−34] Static deuterium NMR measurements have been widely used to study motions in proteins, but it is difficult with this approach to investigate multiple sites simultaneously to extract residue-specific dynamics because of signal overlap.[33] Heteronuclear (^{13}C,^{15}N) dipolar coupling and CSA line shape analysis can also be used to detect internal dynamics in proteins by solid-state NMR. For an axially symmetric dipolar interaction, the ratio of the motionally narrowed dipolar coupling to the rigid-limit coupling is defined as the order parameter. In the ideal rigid environment in the absence of molecular dynamics, the order parameter is 1, while 0 represents the fully motionally averaged isotropic orientation. The dipolar order parameter is thus a measure of the amplitude of the rotation of the internuclear bond vector. In the case of CSA, the correlation time giving rise to the fast limit motions that would reduce the anisotropic line width depends on the nucleus type and on the static magnetic field.

In the past decade, the advances in the preparation of uniformly and differentially enriched protein samples for solid-state NMR spectroscopy[35−42] and the development of the dipolar or/and J-based multidimensional magic angle spinning (MAS) NMR pulse sequences[43−50] have led to complete resonance assignments[36−40,42,51] and to determination of the full 3D structures[52−57] of several globular proteins. In the meantime, the development of the dipolar recoupling techniques permitting recovery of the anisotropic interactions removed by MAS[58−62] opened the field to site-specific investigations of protein dynamics.[40,62−72] Combining recoupling techniques with mul-

(17) Nicholson, L. K.; Teng, Q.; Cross, T. A. *J. Mol. Biol.* **1991**, *218*, 621–637.
(18) Bogusky, M. J.; Schiksnis, R. A.; Leo, G. C.; Opella, S. J. *J. Magn. Reson.* **1987**, *72*, 186–190.
(19) Gall, C. M.; Cross, T. A.; Diverdi, J. A.; Opella, S. J. *Proc. Nat. Acad. Sci. U.S.A.* **1982**, *79*, 101–105.
(20) Williams, J. C.; McDermott, A. E. *Biochemistry* **1995**, *34*, 8309–8319.
(21) Palmer, A. G.; Williams, J.; McDermott, A. *J. Phys. Chem.* **1996**, *100*, 13293–13310.
(22) Ishima, R.; Torchia, D. A. *Nat. Struct. Biol.* **2000**, *7*, 740–743.
(23) Stone, M. J. *Acc. Chem. Res.* **2001**, *34*, 379–388.
(24) Palmer, A. G. *Chem. Rev.* **2004**, *104*, 3623–3640.
(25) Mittermaier, A.; Kay, L. E. *Science* **2006**, *312*, 224–228.
(26) Jarymowycz, V. A.; Stone, M. J. *Chem. Rev.* **2006**, *106*, 1624–1671.
(27) Kay, L. E. *J. Magn. Reson.* **2005**, *173*, 193–207.
(28) Hiyama, Y.; Niu, C. H.; Silverton, J. V.; Bavoso, A.; Torchia, D. A. *J. Am. Chem. Soc.* **1988**, *110*, 2378–2383.
(29) Jelinski, L. W.; Sullivan, C. E.; Torchia, D. A. *Nature* **1980**, *284*, 531–534.
(30) Torchia, D. A. *Methods Enzymol.* **1982**, *82*, 174–186.
(31) Tuzi, S.; Shinzawaitoh, K.; Erata, T.; Naito, A.; Yoshikawa, S.; Saito, H. *Eur. J. Biochem.* **1992**, *208*, 713–720.
(32) Copie, V.; McDermott, A. E.; Beshah, K.; Williams, J. C.; Spijker-assink, M.; Gebhard, R.; Lugtenburg, J.; Herzfeld, J.; Griffin, R. G. *Biochemistry* **1994**, *33*, 3280–3286.
(33) Huster, D. *Prog. Nucl. Magn. Reson. Spectrosc.* **2005**, *46*, 79–107.
(34) Krushelnitsky, A.; Reichert, D. *Prog. Nucl. Magn. Reson. Spectrosc.* **2005**, *47*, 1–25.
(35) McDermott, A.; Polenova, T.; Bockmann, A.; Zilm, K. W.; Paulsen, E. K.; Martin, R. W.; Montelione, G. T. *J. Biomol. NMR* **2000**, *16*, 209–219.
(36) Bockmann, A.; Lange, A.; Galinier, A.; Luca, S.; Giraud, N.; Juy, M.; Heise, H.; Montserret, R.; Penin, F.; Baldus, M. *J. Biomol. NMR* **2003**, *27*, 323–339.
(37) Marulanda, D.; Tasayco, M. L.; Cataldi, M.; Arriaran, V.; Polenova, T. *J. Phys. Chem. B* **2005**, *109*, 18135–18145.
(38) Marulanda, D.; Tasayco, M. L.; McDermott, A.; Cataldi, M.; Arriaran, V.; Polenova, T. *J. Am. Chem. Soc.* **2004**, *126*, 16608–16620.
(39) Yang, J.; Paramasivan, S.; Marulanda, D.; Cataidi, M.; Tasayco, M. L.; Polenova, T. *Magn. Reson. Chem.* **2007**, *45*, S73–S83.
(40) Franks, W. T.; Zhou, D. H.; Wylie, B. J.; Money, B. G.; Graesser, D. T.; Frericks, H. L.; Sahota, G.; Rienstra, C. M. *J. Am. Chem. Soc.* **2005**, *127*, 12291–12305.
(41) Siemer, A. B.; Ritter, C.; Ernst, M.; Riek, R.; Meier, B. H. *Angew. Chem., Int. Ed.* **2005**, *44*, 2441–2444.
(42) Igumenova, T. I.; McDermott, A. E.; Zilm, K. W.; Martin, R. W.; Paulson, E. K.; Wand, A. J. *J. Am. Chem. Soc.* **2004**, *126*, 6720–6727.
(43) Verel, R.; Ernst, M.; Meier, B. H. *J. Magn. Reson.* **2001**, *150*, 81–99.
(44) Hohwy, M.; Rienstra, C. M.; Griffin, R. G. *J. Chem. Phys.* **2002**, *117*, 4973–4987.
(45) Bennett, A. E.; Rienstra, C. M.; Auger, M.; Lakshmi, K. V.; Griffin, R. G. *J. Chem. Phys.* **1995**, *103*, 6951–6958.
(46) Chen, L. L.; Olsen, R. A.; Elliott, D. W.; Boettcher, J. M.; Zhou, D. H. H.; Rienstra, C. M.; Mueller, L. J. *J. Am. Chem. Soc.* **2006**, *128*, 9992–9993.
(47) Linser, R.; Fink, U.; Reif, B. *J. Magn. Reson.* **2008**, *193*, 89–93.
(48) Lesage, A.; Auger, C.; Caldarelli, S.; Emsley, L. *J. Am. Chem. Soc.* **1997**, *119*, 7867–7868.
(49) Takegoshi, K.; Nakamura, S.; Terao, T. *Chem. Phys. Lett.* **2001**, *344*, 631–637.
(50) Chen, L.; Kaiser, J. M.; Polenova, T.; Yang, J.; Rienstra, C. M.; Mueller, L. J *J. Am. Chem. Soc.* **2007**, *129*, 10650−+.
(51) Pauli, J.; Baldus, M.; van Rossum, B.; de Groot, H.; Oschkinat, H. *ChemBioChem* **2001**, *2*, 272–281.
(52) Castellani, F.; van Rossum, B.; Diehl, A.; Schubert, M.; Rehbein, K.; Oschkinat, H. *Nature* **2002**, *420*, 98–102.
(53) Zech, S. G.; Wand, A. J.; McDermott, A. E. *J. Am. Chem. Soc.* **2005**, *127*, 8618–8626.
(54) Lange, A.; Becker, S.; Seidel, K.; Giller, K.; Pongs, O.; Baldus, M. *Angew. Chem., Int. Ed.* **2005**, *44*, 2089–2092.
(55) Franks, W. T.; Wylie, B. J.; Schmidt, H. L. F.; Nieuwkoop, A. J.; Mayrhofer, R. M.; Shah, G. J.; Graesser, D. T.; Rienstra, C. M. *Proc. Natl. Acad. Sci. U.S.A.* **2008**, *105*, 4621–4626.
(56) Loquet, A.; Bardiaux, B.; Gardiennet, C.; Blanchet, C.; Baldus, M.; Nilges, M.; Malliavin, T.; Boeckmann, A. *J. Am. Chem. Soc.* **2008**, *130*, 3579–3589.
(57) Manolikas, T.; Herrmann, T.; Meier, B. H. *J. Am. Chem. Soc.* **2008**, *130*, 3959–3966.
(58) van Rossum, B. J.; de Groot, C. P.; Ladizhansky, V.; Vega, S.; de Groot, H. J. M. *J. Am. Chem. Soc.* **2000**, *122*, 3465–3472.
(59) Hong, M.; Yao, X. L.; Jakes, K.; Huster, D. *J. Phys. Chem. B* **2002**, *106*, 7355–7364.
(60) Chan, J. C. C.; Tycko, R. *J. Chem. Phys.* **2003**, *118*, 8378–8389.
(61) Zhao, X.; Eden, M.; Levitt, M. H. *Chem. Phys. Lett.* **2001**, *342*, 353–361.
(62) Hohwy, M.; Jaroniec, C. P.; Reif, B.; Rienstra, C. M.; Griffin, R. G. *J. Am. Chem. Soc.* **2000**, *122*, 3218–3219.
(63) Huster, D.; Xiao, L. S.; Hong, M. *Biochemistry* **2001**, *40*, 7662–7674.
(64) Lorieau, J. L.; McDermott, A. E. *J. Am. Chem. Soc.* **2006**, *128*, 11505–11512.
(65) Lorieau, J. L.; Day, L. A.; McDermott, A. E *Proc. Natl. Acad. Sci. U.S.A.* **2008**, *105*, 10366–10371.
(66) Chevelkov, V.; Diehl, A.; Reif, B *J. Chem. Phys.* **2008**, *128*.
(67) Chevelkov, V.; Zhuravleva, A. V.; Xue, Y.; Reif, B.; Skrynnikov, N. R. *J. Am. Chem. Soc.* **2007**, *129*, 12594–12595.
(68) Reif, B.; Xue, Y.; Agarwal, V.; Pavlova, M. S.; Hologne, M.; Diehl, A.; Ryabov, Y. E.; Skrynnikov, N. R. *J. Am. Chem. Soc.* **2006**, *128*, 12354–12355.
(69) Giraud, N.; Bockmann, A.; Lesage, A.; Penin, F.; Blackledge, M.; Emsley, L. *J. Am. Chem. Soc.* **2004**, *126*, 11422–11423.
(70) Giraud, N.; Blackledge, M.; Goldman, M.; Bockmann, A.; Lesage, A.; Penin, F.; Emsley, L. *J. Am. Chem. Soc.* **2005**, *127*, 18190–18201.
(71) Kandasamy, S. K.; Lee, D. K.; Nanga, R. P. R.; Xu, J.; Santos, J. S.; Larson, R. G.; Ramamoorthy, A. *Biochim. Biophys. Acta, Biomembr.* **2009**, *1788*, 686–695.
(72) Xu, J. D.; Durr, U. H. N.; Im, S. C.; Gan, Z. H.; Waskell, L.; Ramamoorthy, A. *Angew. Chem., Int. Ed.* **2008**, *47*, 7864–7867.

tidimensional MAS sequences for resonance assignments permits site-specific dynamics studies in uniformly and multiply isotopically labeled proteins, via relaxation and anisotropic line shape analysis.[40,64−67,69,70]

To date, only a few examples have been reported where protein dynamics has been investigated site-specifically by solid-state NMR spectroscopy. Gieaud et al. measured backbone amide ^{15}N spin-lattice relaxation times of Crh using U-^{13}C,^{15}N labeled microcrystalline protein sample and proposed a theoretical model for the quantitative analysis of the MAS NMR longitudinal relaxation time.[69,70] Chevelkov et al. measured ^{15}N T_1 of microcrystalline SH_3 domain of α-spectrin at several magnetic fields using perdeuterated samples.[66] They provided quantitative analysis based on the combination of solid-state and solution NMR T_1 relaxation data and concluded that the relaxation times determined by both methods correlate strongly.[67,68] Huster et al., Lorieau et al., and Franks et al. studied site-specifically the local dynamics of several proteins using ^{1}H−^{13}C and ^{1}H−^{15}N dipolar order parameters.[40,63−65,73,74] In addition, 3D ^{15}N CSA measurements conducted by Wylie et al. showed that backbone dynamics can be probed by recording the ^{15}N CSA tensors.[75] The spin-lattice relaxation time measurements reflect the rate of motion on the time scales of pico- to nanoseconds, whereas ^{1}H−^{13}C and ^{1}H−^{15}N dipolar order parameters and ^{15}N CSA tensors are sensitive to the motional amplitude in the time window of sub-microsecond. To date, there have been no reports of site-specific protein dynamics studied by a combination of relaxation-rate and motional-amplitude measurements performed on the same protein and under the same conditions by solid-state NMR.

In this work, we report backbone amide ^{15}N dynamics in the 1−73 N-terminal fragment of the 1−73(U-^{13}C,^{15}N)/74−108(U-^{15}N) reassembled thioredoxin investigated by combined 2D and 3D MAS NMR measurements of ^{15}N spin-lattice relaxation rates, ^{1}H−^{15}N dipolar order parameters, ^{15}N CSA, as well as the signal intensities in the variable-temperature and amide ^{1}H-T_2'-filtered NCA 2D experiments. Thioredoxin is a 11.7 kDa protein, whose tertiary structure, called a "thioredoxin fold", is composed of five β-sheet and four α-helices. The 3D structures of thioredoxin are available from the X-ray crystallography[76] and solution NMR.[77] The dynamics of the backbone amide ^{15}N atoms of thioredoxin has been extensively studied by solution NMR.[78] In our previous investigations, we obtained resonance assignments of intact and reassembled thioredoxin samples using MAS NMR spectroscopy[37−39] and developed NMR experiments for studies of interfaces of differentially enriched protein assemblies, using thioredoxin as an example.[79] In this report, we present backbone dynamics of thioredoxin on multiple time scales. Analysis of the dynamics parameters based on the measurements of spin-lattice relaxation rates, dipolar order parameters, and CSA line shapes reveals surprising correlations between motions occurring on different time scales, as well as correlations between dynamic behavior and the tertiary structure of the protein. In addition, dynamics parameters from MAS NMR exhibit interesting correlations with the crystallographic B-factors. Finally, dipolar order parameters from MAS NMR measurements and order parameters derived from the Lipari−Szabo analysis of solution NMR relaxation data indicate similar qualitative trends as a function of the residue number. This study demonstrates that the combined measurement of relaxation and anisotropic line shape parameters provides snapshots of thioredoxin dynamics across a wide range of time scales and yields new insights on the correlations between motions occurring on these different time scales. This solid-state NMR approach yields a comprehensive view of dynamics in reassembled thioredoxin and is broadly applicable to other proteins and protein assemblies.

Experimental Section

Sample Preparation. Overexpression and purification protocols for U-^{13}C,^{15}N isotopically enriched thioredoxin were described in previous reports.[38,80] Preparation of differentially enriched 1−73(U-^{13}C,^{15}N)/74−108(U-^{15}N) thioredoxin reassembly was reported in detail previously.[39] In brief, a proteolytic cleavage site was engineered at Arg-73. ^{13}C,^{15}N- and ^{15}N-enriched purified thioredoxin was prepared, and each sample was cleaved into two complementary fragments: one fragment containing the N-terminal residues 1−73 and the other containing the C-terminal residues 74−108. The fragments were purified, and the 1−73(U-^{13}C,^{15}N) fragment was reconstituted with the 74−108(U-^{15}N) fragment. For solid-state NMR experiments, a sample of reassembled 1−73(U-^{13}C,^{15}N)/74−108(U-^{15}N) thioredoxin was prepared by controlled precipitation of 70 mg/mL reassembled thioredoxin in 10 mM phosphate buffer (pH 7.0) from PEG-4000, which is accomplished by the slow addition of a PEG-4000 solution containing 10 mM $NaCH_3COO$ and 1 mM NaN_3 (pH 3.5), as described previously.[38] The sample was centrifuged to remove the supernatant. 11 mg of hydrated thioredoxin precipitate were packed into a 3.2 mm Varian rotor and sealed using an upper spacer and a top spinner.

Solid-State NMR Spectroscopy. All NMR spectra were acquired on a 14.1 T narrow bore Varian InfinityPlus spectrometer equipped with a 3.2 mm triple-resonance T3 MAS probe. The MAS frequency in all experiments was 10 kHz controlled by a Varian MAS controller to within ±0.002 kHz. A $PbNO_3$ temperature sensor was used as a temperature calibration compound for this probe at different MAS frequencies.[81] The actual temperature at the sample was maintained at 288 ± 0.5 K (15 °C) throughout the experiments using the Varian temperature controller, except in the variable-temperature experiments, where additional spectra were acquired at 263 K (−10 °C) and 238 K (−35 °C). ^{1}H, ^{13}C, and ^{15}N chemical shifts were referenced with respect to DSS, with adamantane and ammonium chloride used as external referencing standards.[82] For most of the experiments, the pulse lengths were 2.9 μs (^{1}H), 5 μs (^{13}C), and 5 μs (^{15}N). The ^{1}H-X (X = ^{15}N or ^{13}C) cross-polarization (CP) employed a tangent amplitude ramp (80−100%), the ^{1}H radio frequency field was 50 kHz, and the center of the ramp on the heteronucleus was Hartmann−Hahn matched to the first spinning sideband. The band-selective magnetization transfer from ^{15}N to $^{13}C^{\alpha}$ was realized using 5.2 ms SPECIFIC-CP[83] with tangent amplitude ramp and 27, 17, and 100 kHz RF power in ^{15}N, ^{13}C and ^{1}H, respectively. The ^{1}H decoupling power of ∼80 kHz was

(73) Barre, P.; Yamaguchi, S.; Saito, H.; Huster, D. *Eur. Biophys. J. Biophys. Lett.* **2003**, *32*, 578–584.
(74) Vogel, A.; Katzka, C. P.; Waldmann, H.; Arnold, K.; Brown, M. F.; Huster, D. *J. Am. Chem. Soc.* **2005**, *127*, 12263–12272.
(75) Wylie, B. J.; Franks, W. T.; Rienstra, C. M. *J. Phys. Chem. B* **2006**, *110*, 10926–10936.
(76) Katti, S. K.; Lemaster, D. M.; Eklund, H. *J. Mol. Biol.* **1990**, *212*, 167–184.
(77) Dyson, H. J.; Gippert, G. P.; Case, D. A.; Holmgren, A.; Wright, P. E. *Biochemistry* **1990**, *29*, 4129–4136.
(78) Stone, M. J.; Chandrasekhar, K.; Holmgren, A.; Wright, P. E.; Dyson, H. J. *Biochemistry* **1993**, *32*, 426–435.
(79) Yang, J.; Tasayco, M. L.; Polenova, T. *J. Am. Chem. Soc.* **2008**, *130*, 5798–5807.
(80) Yu, W.; Gibaja, V.; Arevalo, E.; Petit, M. C.; Li, J. H.; Tasayco, M. L. *Biophys. J.* **1997**, *72*, Wp386–Wp386.
(81) Neue, G.; Dybowski, C. *Solid State Nucl. Magn. Reson.* **1997**, *7*, 333–336.
(82) Morcombe, C. R.; Zilm, K. W. *J. Magn. Reson.* **2003**, *162*, 479–486.
(83) Baldus, M.; Petkova, A. T.; Herzfeld, J.; Griffin, R. G. *Mol. Phys.* **1998**, *95*, 1197–1207.

typically used during the acquisition and evolution periods in the 2D and 3D experiments.

For the ^{15}N spin-lattice relaxation time (T_1) measurement, a basic 2D NCA experiment was modified with the 90-τ-90 element inserted following the ^{1}H/^{15}N CP and before the ^{15}N t_1 evolution period.[69] The relaxation curves were acquired using the delays of 0.1, 1, 3, 7, and 15 s. To compensate for the minor instability of the amplifiers and for the slight detuning of the probe during the 2D measurements, we acquired 2D NCA spectra with a 0.1 s longitudinal delay before and after every measurement and renormalized the intensity of the resolved peaks according to the average intensity of the peaks in these control spectra, following previous reports.[69,70]

In the 3D DIPSHIFT experiments, the DIPSHIFT dipolar recoupling period[84] was incorporated into the basic 2D NCA sequence; this combination permits to resolve cross peaks for individual residues. In DIPSHIFT, an RN-type recoupling block, $R18_{17}$,[61] was employed for the recoupling of the ^{1}H$-^{15}$N dipolar coupling and at the same time for the suppression of the ^{1}H$-^1$H homonuclear dipolar interactions.

For the recoupling of the ^{15}N CSA, a 3D ROCSA experiment was conducted.[60,75] For the ROCSA period, a $C2_{21}$ POST block was used with $(a, b) = (0.0329, 0.467)$ and 1 rotor period (100 μs) increment per t_1 point. During ROCSA, a 10 μs ^{13}C π pulse with XY-8 phase cycling scheme[85] was introduced in the middle of every rotor period on the ^{13}C channel, and 110 kHz CW decoupling was employed on the ^{1}H channel. Haeberlen−Mehring−Spiess convention is followed in the definition of the CSA tensor. δ_{iso} is the isotropic chemical shift defined as $\delta_{iso} = 1/3(\delta_{xx} + \delta_{yy} + \delta_{zz})$. δ_{xx}, δ_{yy}, and δ_{zz} are the principal components of the CSA tensor defined as $|\delta_{zz} - \delta_{iso}| \geq |\delta_{xx} - \delta_{iso}| \geq |\delta_{yy} - \delta_{iso}|$. δ_σ is the reduced anisotropy of the CSA tensor determining the breadth of the tensor (throughout the text, we will refer to δ_σ as anisotropy) defined as $\delta_\sigma = \delta_{zz} - \delta_{iso}$, and η is the asymmetry parameter of the CSA tensor determining the deviation from the axial symmetry, defined as $\eta_\sigma = (\delta_{yy} - \delta_{xx})/(\delta_{zz} - \delta_{iso})$.

The chemical shift assignments of 1−73(U-^{13}C,^{15}N)/74−108(U-^{15}N) reassembled thireodoxin have been reported by us previously.[39] Nearly complete backbone and side chain assignments have been made except for residues at the N-terminus including S1, D2, and K3.

Data Processing and Analysis. All spectra were processed in NMRpipe[86] and analyzed in Sparky.[87] 90° or 60° shifted sine bell followed by a Lorentzian-to-Gaussian transformation were applied in both dimensions; forward linear prediction to twice the number of the original data points was employed in the indirect dimension followed by zero filling to twice the total number of points prior to Fourier transformation and phasing.

The chemical shift values and cross peak intensities in the 2D NCA spectra were obtained automatically in Sparky. The ^{15}N$-^1$H dipolar and ^{15}N CSA line shapes in 3D spectra were extracted from the 2D NCA planes using the automatic peak picking procedure *"autofit"* in nmrPipe.

The spin-lattice relaxation curves corresponding to the individual residues were obtained from five 2D NCA experiments with varying spin-lattice relaxation delays (see above) and subsequently fitted to the following equation $I = I_0 \exp(-R_1 t)$, assuming monoexponential decays (as justified by the experimental data). The uncertainty in the R_1 values was estimated from the standard errors of the fitting. The H−N dipolar coupling constants were extracted by the numerical simulations of the dipolar line shapes using SPINEVOLUTION.[88] The ^{15}N CSA line shapes were simulated in SPINEVOLUTION using two-parameter fits, with chemical shift anisotropy, δ_σ, and asymmetry parameter, η, being adjustable parameters. The first guess values were derived from the visual inspection of the lineshapes. Subsequently, a 20 × 20 grid was constructed from 20 δ_σ values using an increment of 1 ppm and 20 η values using an increment of 0.01, and calculations were performed to yield the minimal χ^2. A contour plot of χ^2 as a function of δ_σ and η was built to get the best-fit values of δ_σ with minimum χ^2. The uncertainties associated with δ_σ and η were estimated from the corresponding values of δ_σ and η giving $\chi^2 = 2\chi_{min}^2$.[89]

Results

Temperature Dependence of Heteronuclear NCA Correlation Spectra. A broad-range temperature screen is typically performed for identification of optimal resolution and sensitivity of the MAS NMR spectra in microcrystalline proteins. When solvent translational diffusion or fluctuating motions occur at rates comparable to the frequencies of MAS and/or ^{1}H decoupling, which are typically in the range of 10−100 kHz, these motions interfere with MAS and/or proton decoupling, leading to broadening of the NMR signals and significant intensity loss. In addition, large-amplitude motions with correlation times shorter than the inverse of the X-H dipolar coupling cause a decrease of the $T_{1\rho}$ of the ^{1}H and X spins and a reduction of the H-X cross-polarization efficiency. The broadening of the signals and the suppression of the intensity are therefore a qualitative manifestation of the presence of motions occurring on the time scales of 10−100 μs and <100 μs, in the absence of static conformational heterogeneity.

We have acquired a series of temperature-dependent 2D NCA spectra of the 1−73(U-^{13}C,^{15}N)/74−108(U-^{15}N) reassembled thioredoxin at 238 K (−35 °C), 263 K (−10 °C), and 288 K (15 °C). Figure 1a shows the overlay of the NCA spectra collected at 288 (15 °C) and 238 K (−35 °C) to illustrate the observed changes in chemical shifts and/or intensities. These changes are quantified as a function of the residue number for those peaks that are resolved in the spectra: the backbone amide ^{15}N chemical shift changes $\Delta\delta$ ($\delta_{288K} - \delta_{238K}$) are shown in Figure 1b, and the corresponding peak intensity ratios (intensity$_{288K}$/intensity$_{238K}$) are displayed in Figure 1c. The average ^{15}N chemical shift changes observed between these two temperatures were ∼0.5 ppm. Notably, for 13 of the 45 resolved peaks the chemical shift differences exceed 0.5 ppm. For residues located at the termini of individual α-helices or β-strands (such as I4, C35, I38, L53 in α2, T66 in α3, as well as T54 and L58 in β3), $\Delta\delta$ exceed 0.5 ppm. For I4, I38, L53 and G65, $\Delta\delta$ are greater than 1 ppm. The backbone amide ^{15}N chemical shift is very sensitive to the change in the local conformation, and the 0.5 ppm difference in the ^{15}N chemical shifts between these two temperatures indicates such conformational change takes place.

Upon reducing the temperature from 288 to 238 K, significant reductions in the cross-peak intensities are observed for different residues, indicating the presence of dynamics on the time scales causing interference with MAS and/or decoupling. Inspection of Figure 1c reveals that only a few relatively short stretches are not significantly affected by this motion. These are residues in β2 (23−27), at the terminus of α2 (47), on the N-terminus side of β3 (53−56), and several residues in α3 (64−67). Moderate intensity-reduction ratios between 1.5 and 3 are seen

(84) Munowitz, M.; Aue, W. P.; Griffin, R. G. *J. Chem. Phys.* **1982**, *77*, 1686–1689.
(85) Holl, S. M.; Mckay, R. A.; Gullion, T.; Schaefer, J. *J. Magn. Reson.* **1990**, *89*, 620–626.
(86) Delaglio, F.; Grzesiek, S.; Vuister, G. W.; Zhu, G.; Pfeifer, J.; Bax, A. *J. Biomol. NMR* **1995**, *6*, 277–293.
(87) Goddard, T. D.; Kneller, D. G. *SPARKY 3*; University of California, San Francisco: San Francisco, CA.
(88) Veshtort, M.; Griffin, R. G. *J. Magn. Reson.* **2006**, *178*, 248–282.
(89) Brouwer, D. H.; Enright, G. D. *J. Am. Chem. Soc.* **2008**, *130*, 3095–3105.

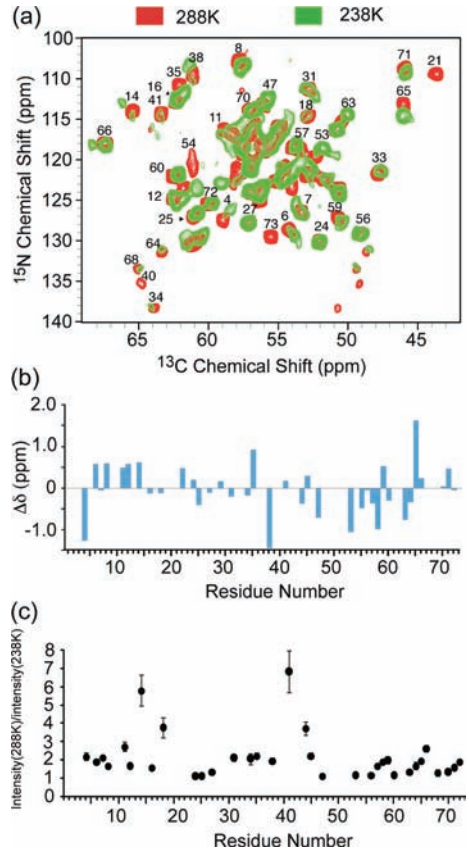

Figure 1. (a) NCA 2D spectra acquired at 238 K (−35 °C) (green) and 288 K (15 °C) (red). The spectra were acquired with 128 points (spectral width of 6 kHz) in the indirect dimension and 1024 points (spectral width of 50 kHz) in the direct dimension, with 128 scans per row. Note that not all resolved peaks are labeled in the figure. (b) ^{15}N chemical shift changes from 2D NCA spectra acquired at temperatures of 238 (−35 °C) and 288 K (15 °C), as a function of the residue number. The mean difference is 0.51 ± 0.5 ppm. (c) Intensity ratio of the 2D NCA cross peaks from the spectra acquired at 238 (−35 °C) and 288 K (15 °C) as a function of residue number.

from the N-terminus until β2, including α1 and β1, and a number of residues in α2 (31−45), on the C-terminus side of β3 (57−59), and in the loop connecting β3 and α3 (64−66), as well as at the C-terminus. Several peaks are reduced in intensity by more than four times, e.g., T14 in α1, K18 in the turn connecting α1 and β2, and I41 and E44 in α2. Most striking is the complete loss of intensity at 238 K for G21 at the terminus of β2, P40 in α2, T54 in β3, and R73 at the C-terminus (see caption of Figure 1c). At the same time, line broadening was observed for some residues. The ^{15}N line widths of I4, L7, T8, F12, T14, K18, I41, L58, T66, and Y70 are more than 90 Hz in the 238 K (−35 °C) spectrum. I41 exhibits the broadest line of 227 Hz, leading to the highest intensity suppression at 238 K (−35 °C) (Figure 1c). These line broadenings and attenuated intensities imply the interference of dynamics with the MAS and/or ^{1}H decoupling during the NMR experiments, indicating the presence of motions at frequencies of 10 to 100 kHz, namely, on the time scale between 100 to 10 μs at 238 K (−35 °C).

***T_2'*-Filtered 2D NCA Experiments.** A proton T_2' filter was inserted prior to the ^{15}N cross-polarization step in the 1D CPMAS and 2D NCA experiments to detect the mobility of the backbone amide protons, as shown in Figure 2a and in Figure S1, Supporting Information, respectively. The $\tau-\pi-\tau$ echo without decoupling during the τ delay can be used to rapidly dephase the proton magnetization in the rigid environment of

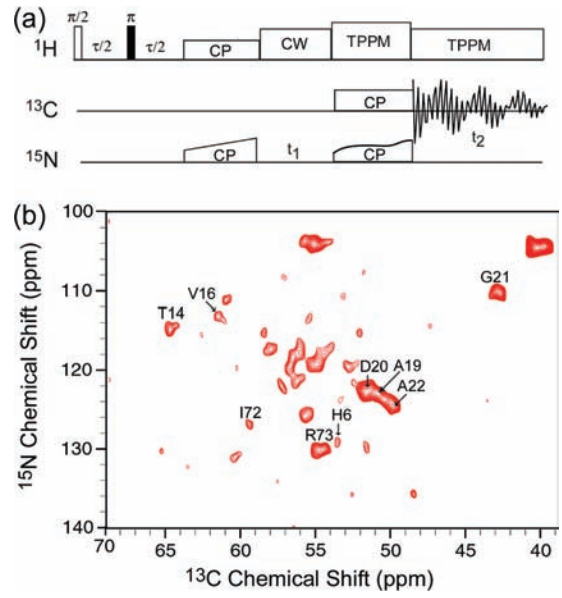

Figure 2. (a) Pulse sequence for ^{1}H T_2'-filtered NCA 2D experiment. (b) NCA 2D spectrum with the 400 μs T_2' filter. The spectrum was acquired with 80 points (spectral width of 6 kHz) in the indirect dimension and 1024 points (spectral width of 50 kHz) in the direct dimension, with 1000 scans per row.

the solid protein.[90] T_2' here refers to the T_2 measured by a spin−echo sequence with a π pulse inserted in the middle of the T_2 decay period to refocus the B_0 inhomogeneity. The magnetization of the protons with longer T_2' can survive the filter and be subsequently transferred to the amide ^{15}N. We conducted a series of proton T_2'-filtered ^{15}N CP experiments with different τ delays. As shown in the 1D spectrum of Figure S1 in Supporting Information, when a 1 ms τ delay was employed, only the side chain ^{15}N signals were observed and no backbone amide ^{15}N signals were detected. Protons of mobile water molecules were reported to be able to survive the T_2' filter that is several milliseconds long and exchange hydrogens to neighboring amine and hydroxyl groups of the protein on a millisecond time scale.[91] Therefore, the side chain ^{15}N signals that survive the 1 ms T_2' filter in the ^{15}N CP experiment in reassembled thioredoxin are attributed to the ^{15}N spins accessible to the mobile water molecules. Our observation of the accessibility of side chain ^{15}N atoms and nonaccessibility of backbone amide ^{15}N atoms by mobile water in the T_2'-filtered 1D ^{15}N CP spectra is well consistent with the previous reports.[91] It is important to note that the results of the 1D T_2'-filtered ^{15}N CP experiments exclude the possibility of exchange between backbone amide protons and mobile water in the proton T_2'-filtered 2D NCA spectra, discussed in the next paragraph.

In the 2D NCA spectrum acquired with 200 μs T_2' delay (not shown), the cross peak intensities were found to decrease significantly. Signals from all four proline residues and from G65 are completely lost as a result of the low ^{1}H/^{15}N CP efficiency for proline residues or relatively short T_2' of amide ^{1}H atom in G65. The 2D NCA spectrum collected with a 400 μs T_2' delay is shown in Figure 2b. The signals at ∼104.2 ppm in the spectra correspond to the folded water-exchangeable side chain signals (the actual chemical shift of those is ∼35 ppm),

(90) Harbison, G. S.; Roberts, J. E.; Herzfeld, J.; Griffin, R. G. *J. Am. Chem. Soc.* **1988**, *110*, 7221–7223.
(91) Bockmann, A.; Juy, M.; Bettler, E.; Emsley, L.; Galinier, A.; Penin, F.; Lesage, A. *J. Biomol. NMR* **2005**, *32*, 195–207.

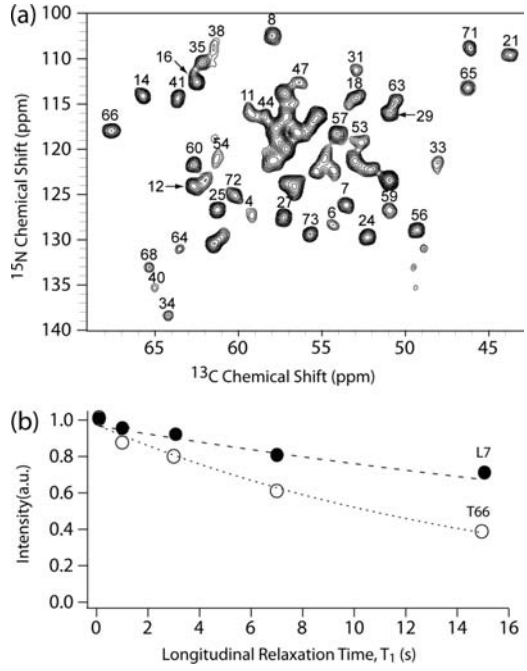

Figure 3. (a) 2D NCA spectrum acquired with a 0.1 s delay during the spin-lattice relaxation period. The spectrum was acquired with 128 points (spectral width of 6 kHz) in the indirect dimension and 1024 points (spectral width of 50 kHz) in the direct dimension, with 64 scans per row. (b) Representative T_1 relaxation curves for L7 and T66.

which is demonstrated by the previous ^{15}N CP experiment employing a 1 ms T_2' filter (Figure S1, Supporting Information). The majority of the peaks were filtered out in the spectrum by a 400 μs proton T_2' dephasing period. Using our existing ^{15}N and C$^{\alpha}$ chemical shift assignments for this sample, we can assign several isolated peaks in the spectrum. Signals in the chemical shift range of 54−60 ppm in the ^{13}C$^{\alpha}$ dimension and those in the range of 116−127 ppm in the ^{15}N dimension are difficult to assign in the current 2D spectrum because of the cross peak overlap. Among the assigned peaks, signals from A19, D20, G21, and R73 are present with relatively high intensity. Other signals from H6, T14, V16, and I72 are also present but their intensities are significantly attenuated. The survival of the above signals undoubtedly indicates longer T_2' of the amide protons, and high mobility of the corresponding residues on the submillisecond time scale because ^{1}H T_2 is sensitive to the motion on the corresponding time scales. However, the spectral intensities are compromised as a result of the magnetization dephasing by the T_2' filter. Additional intensity attenuations were observed for those residues with low ^{1}H/^{15}N CP and ^{15}N/^{13}C SPECIFIC CP efficiency in NCA, even when these residues have relatively long ^{1}H T_2'.

^{15}N Spin-Lattice Relaxation Rates. To probe motions on the pico- to nanosecond time scale, we conducted ^{15}N T_1 measurements. We employed a pulse sequence for the site-specific T_1 measurement that incorporates a longitudinal relaxation delay into an NCA sequence, as introduced previously.[69] The 2D NCA spectrum with 0.1 s longitudinal delay is shown in Figure 3a. 38 of the 73 signals are resolved well enough to allow the intensities of these peaks to be used for the subsequent residue-specific analysis of the relaxation data. The relaxation curves were generated from the spectra acquired with the longitudinal delays of 0.1, 1, 5, 7, and 15 s: for each residue the cross peak intensities were plotted as a function of the delay time, and the experimental points were fitted to a single-exponential function

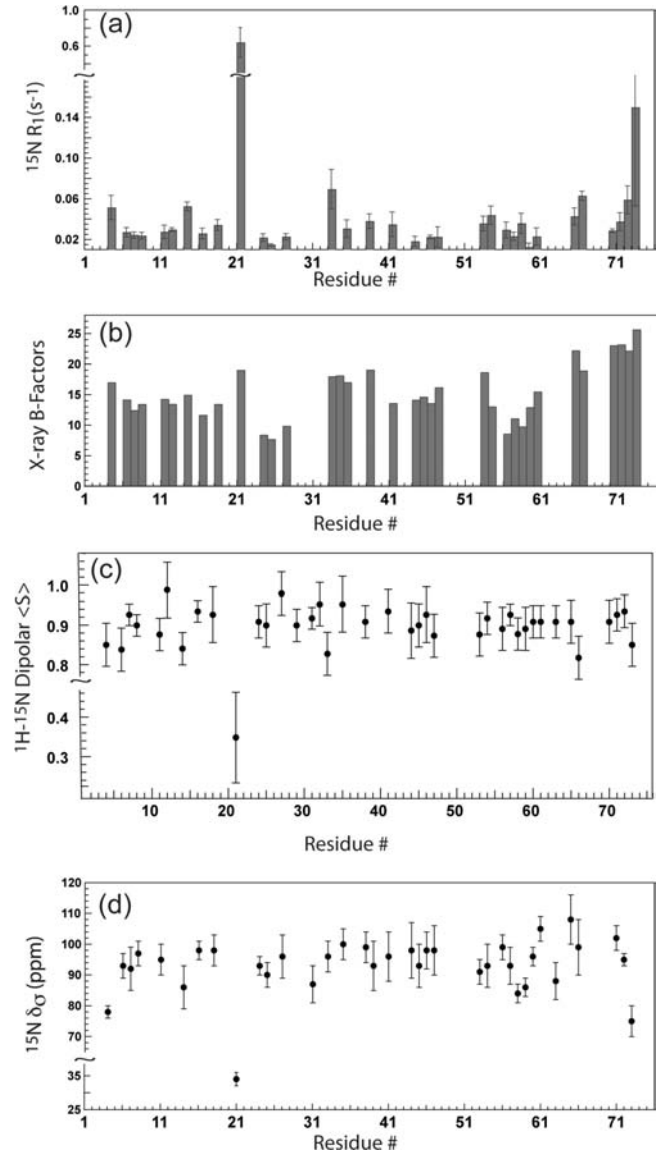

Figure 4. Experimental NMR observables of protein dynamics, plotted as a function of the residue number for reassembled *E. coli* thioredoxin. (a) ^{15}N R_1 relaxation rate constants (solid-state NMR, this work). (b) Crystallographic B factors for residues 1−73 of full-length thioredoxin (X-ray diffraction, lit. data[76]). (c) ^{1}H−^{15}N dipolar order parameters $\langle S \rangle$ (solid-state NMR, this work). (d) ^{15}N chemical shift anisotropy δ_σ (solid-state NMR, this work).

to extract the residue-specific relaxation rates R_1. Figure 3b shows two typical longitudinal delay curves. For several resolved signals, we could not obtain R_1 because of poor signal-to-noise ratio at the spectra with T_1 delays; these residues were not used in the subsequent analysis.

As shown in Figure 4a, the R_1 of thioredoxin were observed in the range from 0.012 to 0.636 s^{-1} (the corresponding T_1 of 83 and 1.6 s) with the average of 0.054 ± 0.008 s^{-1}. The broad range of the R_1 values indicates large variations in the dynamic behavior on the pico- to nanosecond time scales for different residues in the solid reassembled thioredoxin, which is in contrast with the mild variations in the R_1 values of thioredoxin measured by solution NMR.[78] In solution NMR, the variation of T_1 values in the 1−73 fragment is from 0.38 to 0.72 s, showing the dominating influence of the overall tumbling to the internal motions of the protein on the pico- to nanosecond time scale.

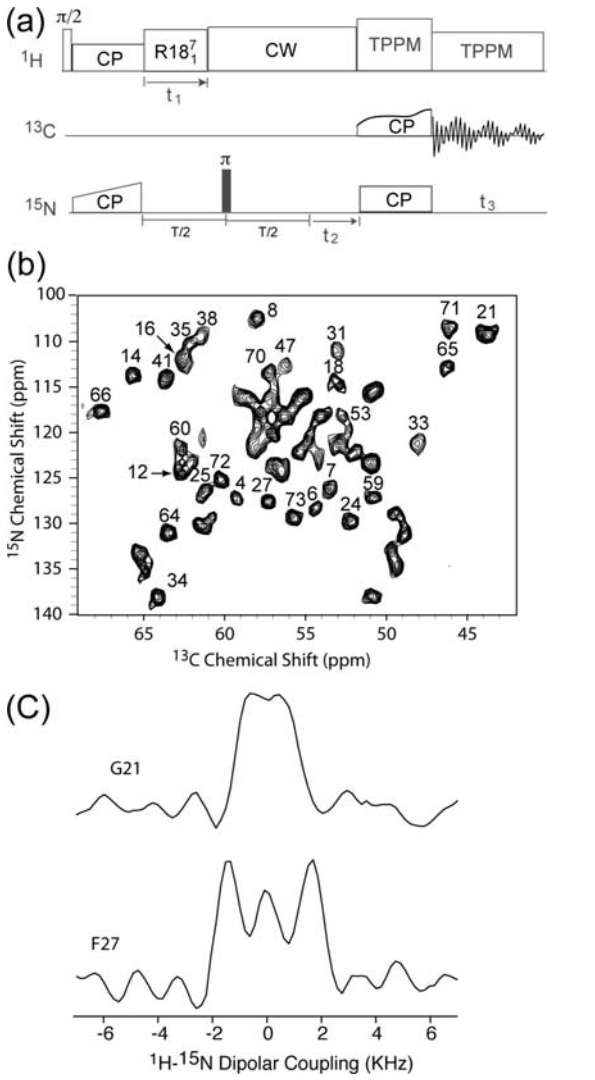

Figure 5. (a) Pulse sequence for the 3D DIPSHIFT experiment. (b) First NCA plane of the DIPSHIFT 3D spectra. The 3D spectrum was acquired with 64 points (spectral width of 45 kHz) in the indirect t_1 dimension (^{1}H−^{15}N dipolar dimension), 80 points (spectral width of 6 kHz) in the indirect t_2 dimension (^{15}N chemical shift dimension), and 1024 points (spectral width of 50 kHz) in the direct dimension, with 32 scans per row. The total measurement time is ∼4 days. (c) Representative ^{1}H−^{15}N dipolar line shapes illustrated for G21 and F27.

Some residues exhibit R_1 values that are significantly higher than mean value. G21 and R73 display the highest relaxation rates. Curiously, these two residues undergo simultaneous motions on the pico- to nanosecond time scale and on the micro- to millisecond time scale: in the variable-temperature and T_2'-filtered NCA spectra discussed previously, these two residues also show the highest mobility. In the variable-temperature NCA experiments, G21 and R73 disappear completely upon lowering the temperature from 288 K (15 °C) to 238 K (−35 °C), whereas in the T_2'-filtered spectrum, these two residues have the highest intensities among the signals that survived. Other residues, such as I4, T14, G33, T66, and I72, have R_1 values significantly higher than average, also implying the high flexibility of these residues on the pico- to nanosecond time scale.

N−H Dipolar Order Parameters. Figure 5a shows the 3D pulse sequence for the measurement of backbone amide H−N dipolar couplings. In this pulse sequence, a DIPSHIFT recoupling period is combined with SPECIFIC-CP in order to obtain the N−H dipolar line shapes in the third dimension with the peaks resolved in the NCA planes. An R-type block was employed for the recoupling the H−N dipolar couplings and for the suppression of the ^{1}H−^{1}H homonuclear dipolar interactions at the same time. In this study, we used the $R18_{17} = \{180_{70}180_{-70}\}_9$ element with 10 kHz MAS spinning frequency. The theoretical scaling factor of $R18_{17}$ recoupling block is 0.315. There are other choices for the H−N recoupling besides the RN block. For example, both T-MREV[62] and LGCP[58,59] have higher scaling factors than the RN-type technique. However, T-TREV requires MAS spinning frequencies <8 kHz, while LGCP has lower sensitivity, and the line shape extracted from LGCP is more sensitive to minor instabilities of the radio frequency (RF) power compared to RN recoupling.

Before carrying out the 3D DIPSHIFT-NCA experiments in reassembled thioredoxin, we tested extensively the performance of the pulse sequence. First, we examined the 3D pulse sequences by comparing the N−H dipolar coupling derived from the ^{13}C-detected 3D DIPSHIFT and the ^{15}N-detected 2D DIPSHIFT experiments using the U-^{13}C,^{15}N MLF peptide sample. The differences in dipolar couplings extracted from these measurements were found to be within the experimental uncertainty. We also tested the dependence of the scaling factor on the ^{1}H RF power mis-set during the RN recoupling. We found that when the ^{1}H RF power was mis-set by −7 and +6 kHz from the RF power value required for the recoupling of the N−H dipolar coupling, −13% and +10% offsets in the scaling factors were observed, respectively. This result is in complete agreement with the previous study by Zhao et al.[92] The other source of uncertainty in the N−H dipolar order parameters is the uncertainty in the simulations of the outer peaks of the line shape; in this work, 0.2−0.5 kHz uncertainty in the N−H dipolar coupling constant is estimated. The resulting overall uncertainty in the N−H order parameter is 0.03−0.07. It should be noted that the actual scaling factor of the outer peaks of the line shape may be systematically lower than the theoretical scaling factor, so it is necessary to calibrate the actual scaling factor if the dipolar coupling is extracted from the measurement of the splitting of the outer peaks of the line shape.

The first 2D NCA plane of the 3D DIPSHIFT spectrum is shown in Figure 5b; 41 peaks are resolved in this spectrum. Dipolar N−H lineshapes for these peaks were exacted in the third dimension, and we obtained a total of 37 N−H order parameters; for four proline residues with no direct amide N−H bond, no N−H dipolar order parameters exist. Figure 5c shows as an example the N−H dipolar line shape for two residues, G21 and F12, illustrating the large variation of the N−H dipolar couplings. The reduced N−H dipolar coupling constants for all residues were directly extracted from these dipolar line shapes with the assumption of $\langle\eta\rangle = 0$. The static limit N−H dipolar coupling constant 11.34 kHz was employed in the calculation of the N−H dipolar order parameters.[93]

We plotted the order parameters against the residue number in Figure 4c. The amide N−H order parameters for reassembled thioredoxin span the range from 0.35 ± 0.11 to 0.99 ± 0.07, with the average of 0.89 ± 0.06 (average H−N dipolar coupling constant 10070 ± 680 Hz). It should be noted that the average backbone order parameters vary between different proteins. For example, in the microcrystalline globular ubiquitin the average (^{13}C^{1}H)α order parameter was reported to be 0.80 ± 0.06,[64]

(92) Zhao, X.; Sudmeier, J. L.; Bachovchin, W. W.; Levitt, M. H. *J. Am. Chem. Soc.* **2001**, *123*, 11097–11098.
(93) Yao, L. S.; Vogeli, B.; Ying, J. F.; Bax, A. *J. Am. Chem. Soc.* **2008**, *130*, 16518–16520.

whereas in the coat protein of Pf1 bacteriophage the ($^{13}C^{1}H$)α order parameter was measured to be 0.99 ± 0.04 using the same LGCP-DARR 3D method.[57]

Among the residues with resolved cross peaks, the most flexible one is G21, which is located at the terminus of the β2 sheet. Other residues in turns and at the termini, such as G33, also display order parameters lower than the average values. In addition, several residues located in α-helices and β-strands also exhibit high mobility. These residues, H6, T14 are located in β1, α1 and have order parameters of 0.84 ± 0.05, and 0.84 ± 0.04, respectively. The most static residues F12 and F27 are located in α2 and β2 and have order parameters of 0.99 ± 0.07 and 0.98 ± 0.05, respectively.

^{15}N Chemical Shift Anisotropy Tensors. ^{15}N chemical shift anisotropy is another NMR parameter that is sensitive to protein dynamics. In the presence of motions occurring at frequencies faster than the magnitude of the CSA interaction, the chemical shift anisotropy is reduced. The ratio of the anisotropy in the presence of motion to the static-limit anisotropy is a probe of dynamics. ^{15}N CSA at 14.1 T is in the range of ca. 10 kHz, and therefore it is sensitive to the motions occurring on the time scales of less than 100 μs. In uniformly enriched proteins, chemical shift anisotropy tensors can be measured either by conducting low-frequency MAS experiments[94] with subsequent Herzfeld−Berger analysis of the spinning sideband intensities[95] or by using the ROCSA recoupling method[60] that permits efficient CSA recoupling at spinning frequencies higher than 10 kHz. For sensitivity reasons, ROCSA is the desired approach under our experimental conditions. To ensure site-specific resolution, we conducted a 3D ROCSA-NCA experiment. The influence of SPECIFIC-CP on the reorientation of the CSA tensor in a 3D experiment was addressed previously.[75] In that work, the differences in line shapes were found to be small between the ^{1}H−^{15}N ^{15}N-detected 2D and the ^{13}C-detected 3D experiments. We additionally tested the $C2_{21}$ ROCSA recoupling block under different MAS spinning frequencies, using crystalline valine as a control sample. The anisotropy and the asymmetry parameter of the CSA tensor, δ_σ and η, for the carbonyl carbon in our measurement are consistent with the literature values.[96]

As shown in Figure 6a, 45 cross peaks are resolved in the 2D NCA plane of the 3D ROCSA-NCA spectrum and 42 ^{15}N CSA line shapes were extracted. Among these residues, 38 were fit with satisfactory rmsd (<5%); for four residues line shapes were not used in the subsequent analysis because of poor signal-to-noise ratio (see Supporting Information). Figure 6b shows the representative experimental and simulated ROCSA line shapes to illustrate the agreement between experiment and simulations.

Figure 4d shows the best fit ^{15}N δ_σ for amide nitrogen atoms plotted against the residue number. The δ_σ values were observed in the range from 34 to 108 ppm, with the average δ_σ of 92.3 ± 5.2 ppm; the average η is 0.21 ± 0.11. There is a pronounced difference in the CSA tensors between residues in α-helices and β-sheets, with an average δ_σ of 95.6 ± 6.0 and 91.6 ± 4.6 ppm and η of 0.19 ± 0.10 and 0.25 ± 0.11 for α-helices and β-sheets, respectively. The differences in the average ^{15}N δ_σ and η for the α-helical and β-sheet structure types were also

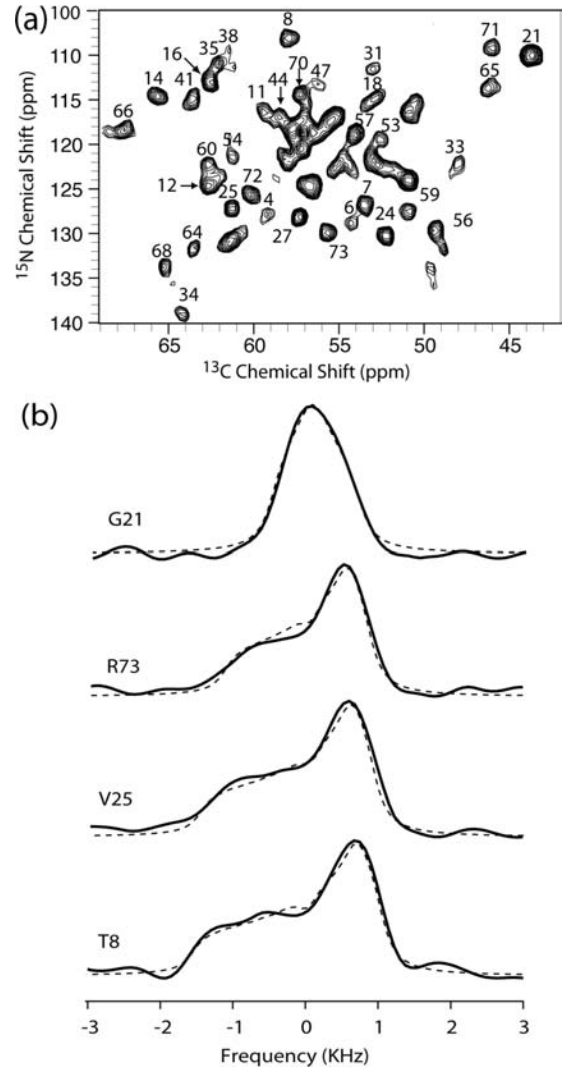

Figure 6. (a) First NCA plane of the ROCSA 3D experiment. The 3D spectrum was acquired with 20 points (spectral width of 10 kHz) in the indirect t_1 dimension (^{15}N ROCSA dimension), 80 points (spectral width of 6 kHz) in the indirect t_2 dimension (^{15}N chemical shift dimension), and 1024 points (spectral width of 50 kHz) in the direct dimension, with 48 scans per row. The total measurement time is ~3.8 days. (b) Representative ^{15}N CSA pseudostatic powder line shapes extracted from the 3D spectrum. The fit values are G21, δ_σ = 34 ± 2 ppm, η = 1.0 ± 0.25; R73, δ_σ = 75 ± 5 ppm, η = 0.16 ± 0.11; V25, δ_σ = 90 ± 4 ppm, η = 0.20 ± 0.10; T8, δ_σ = 97 ± 4 ppm, η = 0.20 ± 0.08.

observed in the previous solution NMR[97−100] and solid-state NMR studies.[75] The average ^{15}N δ_σ value in our measurement is smaller than the reported solution NMR values of 112 ppm,[97−100] The δ_σ values derived from solution NMR measurements were corrected for the effects of internal motion, whereas the corresponding values in this work were extracted directly from the motionally narrowed pseudostatic powder line shape without any correction for the effect of motion.

We next measured the ^{15}N CSA line shapes for the individual residues. The presence of backbone motions is evident for I4,

(94) Wylie, B. J.; Sperling, L. J.; Frericks, H. L.; Shah, G. J.; Franks, W. T.; Rienstra, C. M. *J. Am. Chem. Soc.* **2007**, *129*, 5318–5319.
(95) Herzfeld, J.; Berger, A. E. *J. Chem. Phys.* **1980**, *73*, 6021–6030.
(96) Ye, C. H.; Fu, R. Q.; Hu, J. Z.; Hou, L.; Ding, S. W. *Magn. Reson. Chem.* **1993**, *31*, 699–704.
(97) Cornilescu, G.; Bax, A. *J. Am. Chem. Soc.* **2000**, *122*, 10143–10154.
(98) Kroenke, C. D.; Rance, M.; Palmer, A. G. *J. Am. Chem. Soc.* **1999**, *121*, 10119–10125.
(99) Loth, K.; Pelupessy, P.; Bodenhausen, G. *J. Am. Chem. Soc.* **2005**, *127*, 6062–6068.
(100) Damberg, P.; Jarvet, J.; Graslund, A. *J. Am. Chem. Soc.* **2005**, *127*, 1995–2005.

T14, G21, W31, L58, and R73 residues from their significantly lower than average δ_σ values. G21, whose δ_σ is only 36% of the average value, exhibits an almost symmetric powder line shape and an unusually high η of 1.0 ± 0.25 and is therefore highly mobile. Interestingly, in our previous study[39] we observed that G21 has unusual TALOS-predicted backbone torsion angles (θ, Ψ). On the basis of the current CSA results, we hypothesize that these unusual torsion angles may be attributed to the high mobility of this residue. The almost symmetric line shape (a rhombic CSA tensor) is due to the partial averaging of the different principal values of the CSA tensor by the large-amplitude motion with the correlation time shorter than 100 μs.

Discussion

Dynamics on Different Time Scales. Solid-state NMR spectroscopy is ideally suited for studies of protein motions because in solids the absence of the overall molecular tumbling renders internal dynamics a sole source of modulation of different terms in the spin Hamiltonian and motions can thus be probed on multiple time scales using appropriate NMR observables, yielded by, e.g., relaxation, dipolar, and CSA-based line shape analysis methods. In contrast, the overall molecular tumbling in solution complicates the interpretation of the NMR experiments in terms of specific motional models, especially when the time scales of the overall tumbling and the internal motions are similar. However, the time scale of micro- to milliseconds is particularly important because many biologically relevant events, including signal transduction, enzyme catalysis, and ligand binding, often take place in this range of time scales. Therefore, from the biological point of view, solid-state NMR is specifically suited to study the motions directly related to the functions of the proteins. In this study, we used ^{15}N as a probe of motion and employed various solid-state NMR methods based on variable-temperature measurements, T_2'-filtered experiments, spin-lattice relaxation, CSA, and dipolar interactions to get a comprehensive picture of the backbone dynamics on multiple time scales for reassembled thioredoxin. ^{15}N spin-lattice relaxation is sensitive to the fluctuations occurring near the ^{15}N Larmor frequency, with the correlation times from pico- to nanoseconds. The magnitudes of the ^{1}H−^{15}N dipolar coupling and the ^{15}N CSA are both of the order of 10 kHz, and these two interactions are therefore sensitive to the motions on time scales <100 μs. The intensity variations in the variable-temperature NCA experiments arise due to the motions occurring at frequencies comparable to the MAS and ^{1}H decoupling frequencies, and intensity changes would therefore indicate large-amplitude motions on the time scales of 10−100 μs. The ^{1}H T_2' relaxation is sensitive to the motions in the micro- to millisecond time scales. Therefore, the above measurements in aggregate provide information about molecular dynamics on time scales from pico- to milliseconds.

To gain insight on the molecular motions in reassembled thioredoxin emerging from the various measurements, in Figure 7 we illustrate the variations in the solid-state NMR parameters, R_1, $\langle S \rangle$, δ_σ, chemical shift change $\Delta\delta$ in the variable-temperature experiments, and intensity change in the variable-temperature experiments color-coded for the individual residues in the thioredoxin tertiary structure. We also plot the literature X-ray B-factors[76] and solution NMR generalized order parameters $(S^2)^{0.5}$ (reported in ref 78) in an attempt to develop a general description of molecular motions in thioredoxin as probed by these complementary techniques.

From the aggregate of experimental data summarized in Figure 7, an interesting picture emerges. First, G21 and R73 exhibit the highest mobility among the residues with resolved signals on all time scales and for all experiments we carried out in the solid state, suggesting some degree of correlation between the motions on the different time scales. This observation is in line with the previous reports: the fast librations in the amino acids occurring on the pico- to nanosecond time scales are indeed believed to modulate the slower motions,[21,101] which are often related to specific biological function (e.g., enzyme catalysis[1,3,4]). To assess whether this observation holds quantitatively, i.e., whether the pico- to nanosecond dynamic properties correlate with motions on submicrosecond time scales, we plotted the relaxation rates as a function of the ^{1}H−^{15}N dipolar parameters (Figure 8). Interestingly, for the majority of the residues there is a clear general trend: R_1 increases with the decrease of the order parameter. For example, five of six residues with the R_1 greater than 0.05 s^{-1} have order parameters smaller than 0.85. This trend indicates that residues with larger motional amplitudes on the submicrosecond time scale also have faster fluctuation rates on the pico- to nanosecond time scale. However, there are notable exceptions, for example H6. In H6, the amide nitrogen shows high mobility on the submicrosecond time scale, as evidenced by its low ^{1}H−^{15}N dipolar order parameter of 0.84 ± 0.05. At the same time, this residue does not exhibit high mobility on the pico- to nanosecond time scales, as evidenced by its R_1 of 0.027 ± 0.0047 s^{-1}; this value is lower than the average. Therefore, the motions in this residue occur predominantly on time scales slower than nanoseconds. The other exception is I72; this residue is relatively rigid according to all measurements, except for spin-lattice relaxation experiments revealing shorter-than-average T_1 and indicating dynamics on pico- to nanosecond time scale for this residue.

We have also plotted the ratios of peak intensities in the 2D NCA spectra acquired at 238 K (−35 °C) and 288 K (15 °C) versus the solid-state spin-lattice relaxation rates R_1 and ^{1}H−^{15}N dipolar order parameters $\langle S \rangle$ (see Figure S2, Supporting Information). As discussed in the Experimental Section, comparison of the peak intensities in the 2D NCA spectra acquired at these two temperatures reveals that at 238 K (−35 °C), the intensities corresponding to G21 and R73 (the most mobile residues according to the spin-lattice relaxation and T_2' filter NCA experiment) are completely lost, while several other mobile residues such as T14 and G33 show significant depression of peak intensities, demonstrating the qualitative effect of dynamics on the peak intensity. However, as is clear from Figure S2 in Supporting Information, there are no obvious simple correlations between the absolute intensities at these two temperatures and solid-state R_1 and $\langle S \rangle$.

Additionally, we have examined the chemical shift changes in the variable-temperature experiments as a function of the solid-state R_1 and $\langle S \rangle$. No relations were observed, although several residues with large $\Delta\delta$, such as I4, T14, and L53, also show higher mobility. Other residues in the α-helices and β-sheets, such as C35, I38, D47, L57, also show large $\Delta\delta$. However, these residues are relatively rigid as evidenced by the solid-state R_1 and $\langle S \rangle$.

Relationship between Dynamic Behavior and Structure. Structurally, *E. coli* thioredoxin contains a central core of five β-strands surrounded by four α-helices. In the reassembled

(101) Heberle, J.; Fitter, J.; Sass, H. J.; Buldt, G. *Biophys. Chem.* **2000**, *85*, 229–248.

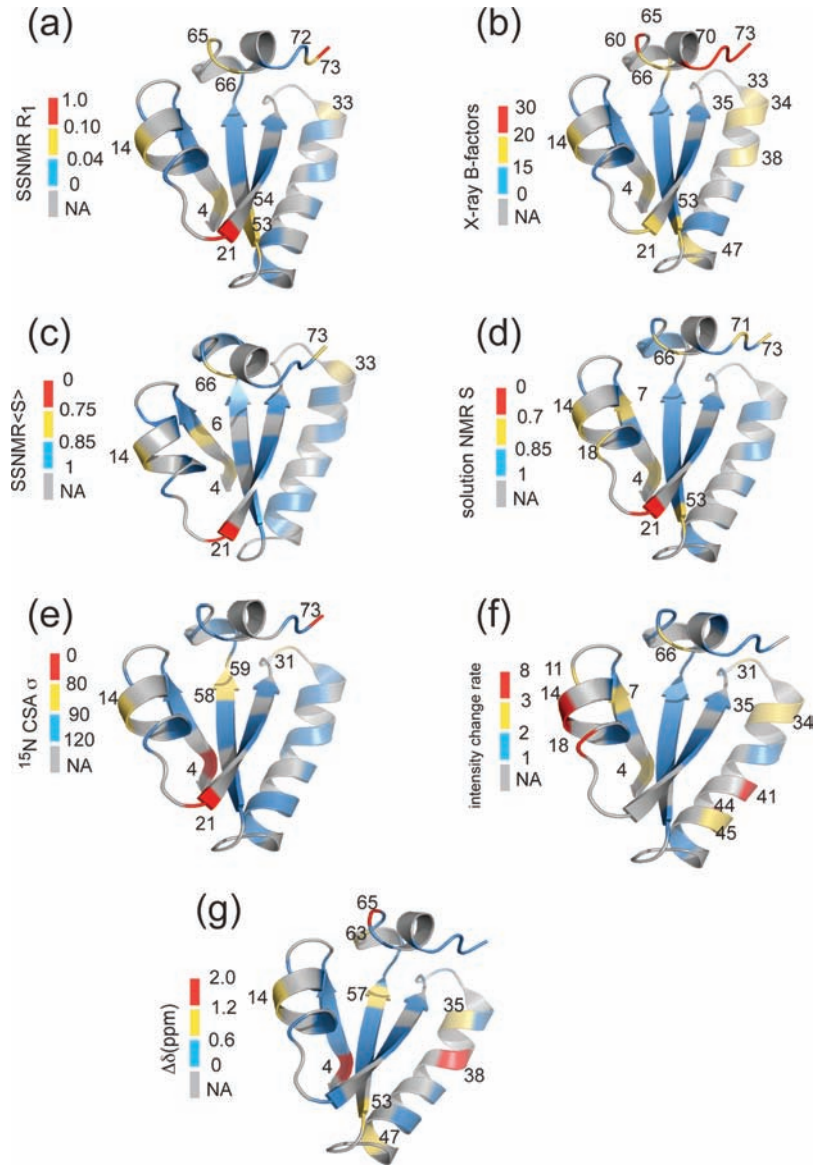

Figure 7. Tertiary structure of the N-terminal (1−73) fragment of reassembled thioredoxin illustrating the dynamic behavior of the individual residues as captured by the different experimental observables (a) Spin-lattice relaxation rate constant R_1 (solid-state NMR, this work). (b) Crystallographic B factor for residues 1−73 of full-length thioredoxin (X-ray diffraction, lit. data[76]). (c) ^{1}H−^{15}N dipolar order parameter $\langle S \rangle$ (solid-state NMR, this work). (d) Solution NMR order parameter $(S^2)^{0.5}$ (solution NMR, lit. data[78]). (e) ^{15}N chemical shift anisotropy δ_σ (solid-state NMR, this work). (f) Cross peak intensity ratio in the 2D NCA experiment acquired at 288 (15 °C) and 238 K (−35 °C) (solid-state NMR, this work); ^{15}N chemical shift change $\Delta\sigma$ in the variable-temperature 2D NCA experiments acquired at 288 (15 °C) and 238 K (−35 °C) (solid-state NMR, this work). Throughout the figure, the largest changes compared with the static case are coded red, moderate changes are yellow, small changes are blue, and residues not addressed because of the spectral congestion are gray.

1−73(U-^{13}C,^{15}N)/74−108(U-^{15}N) thioredoxin complex, the 1−73 fragment is composed of the $\beta\alpha\beta\alpha\beta\alpha\beta$ motif, where β2 in this fragment forms an intermolecular interface with β4 in the complementary 74−108 fragment, and with hydrogen bonds between these two β-strands forming an antiparallel β-sheet. At the cleavage site, R73 is connected to G74 by a hydrogen bond, and the secondary structure of reassembled thioredoxin both in solution and in the solid state is very similar to that of the native full-length thioredoxin, as demonstrated previously by the analysis of the torsion angles in solution and in the solid state[38,39] and by the analysis of NOE contacts.[80]

To identify the correlation between dynamics and structure in reassembled thioredoxin, we compared the average ^{15}N spin-lattice relaxation rates R_1 and order parameters $\langle S \rangle$ of the α-helical and β-strand secondary structure elements, as defined on the basis of the 3D X-ray structure of full-length thioredoxin.[76] Table 1 lists the average ^{15}N R_1, $\langle S \rangle$, and δ_σ values corresponding to the different secondary structures. As described above, the remarkable (∼4 ppm) difference in the ^{15}N chemical shift anisotropy between α-helices and β-strands arises from the differences in the backbone torsion angles rather than the differences in the motions.[102] The mean order parameters for the α-helices and β-sheets are 0.91 ± 0.06 and 0.90 ± 0.06, respectively. This difference is within the standard deviations. The α-helices have a slightly higher average R_1, 0.031 ± 0.006, compared to the β-strands, whose average R_1 is 0.030 ± 0.005. In contrast, there is pronounced difference between the residues

(102) Poon, A.; Birn, J.; Ramamoorthy, A. *J. Phys. Chem. B* **2004**, *108*, 16577–16585.

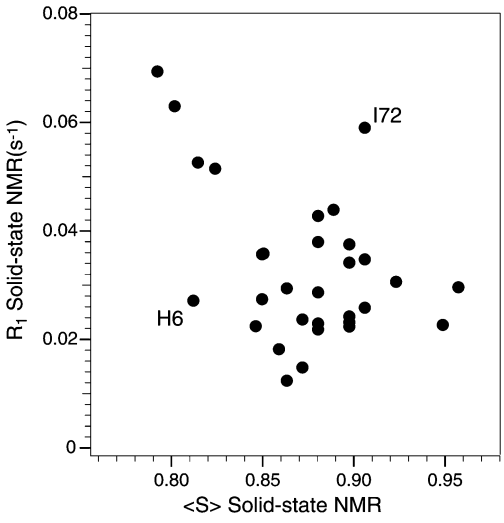

Figure 8. Solid-state dipolar order parameter $\langle S \rangle$ against spin-lattice relaxation rate constant R_1. G21 ($\langle S \rangle = 0.35$, $R_1 = 0.64$) and R73 ($\langle S \rangle = 0.85$, $R_1 = 0.15$) are not plotted because of the limited scale.

Table 1. Average Backbone ^{15}N Solid-State NMR Dynamics Parameters[a]

structural elements	R_1 (s^{-1})	$\langle S \rangle$	δ_σ (ppm)	η_σ
all	0.054 ± 0.008	0.89 ± 0.06	92.3 ± 5.2	0.21 ± 0.11
helix	0.031 ± 0.006	0.91 ± 0.06	95.6 ± 6.0	0.19 ± 0.10
sheet	0.030 ± 0.005	0.90 ± 0.06	91.6 ± 4.6	0.25 ± 0.11
Turn, loop and termini	0.167 ± 0.038	0.80 ± 0.06	85.3 ± 4.6	0.30 ± 0.13

[a] The secondary structure is defined on the basis of the 3D X-ray structure of full-length thioredoxin.[76]

constituting these "regular" secondary structure elements (α-helices and β-sheets) and those found in the "non-regular" secondary structure environments, such as termini, loops, and turns. The average ^{15}N R_1 of the residues located in turns, loops and termini, is 0.167 ± 0.038 s^{-1}, which is significantly higher than that for α-helices and β-sheets (see above). Similarly, the ^{15}N dipolar order parameter in turns, loops and termini is 0.80 ± 0.06, which is lower than the corresponding average for the α-helices and β-strands of 0.91 ± 0.06 and 0.90 ± 0.06, respectively. Higher mobility on the pico- to nanosecond time scale for residues constituting the "non-regular" secondary structure elements was also observed by solution NMR in several proteins.[103]

The most mobile residue among the resolved peaks is G21, whose $\langle S \rangle$ is 39% of the mean value, δ_σ is 37% of the mean value, and R_1 is 20 times higher than the mean value. The neighboring residues, D20 and A22, also show high mobility, which was pronounced in the T_2'-filtered NCA spectra, even though the peaks corresponding to these residues are not resolved in the relaxation and order parameter experiments, and therefore the corresponding observables could not be obtained. In the X-ray structure, residues 20−22 are situated between α1 and β2. However, the geometry of this segment cannot be classified as a normal reverse turn, because the interatomic A19−A22 C^α−C^α distance is greater than the limit defined for a tight turn. In addition, these residues are involved in intra- and intermolecular backbone−backbone hydrogen bonds. The intermolecular G21(O)−N83(N) and A22(N)−K52(O) hydrogen bonds connect β2−β3 and β2−β4, respectively, through water molecules. Meanwhile, the side chain of D20 was reported to form a hydrogen bond with E85 of the complementary fragment.[76] This relatively loose turn geometry and the water-mediated hydrogen bonds are likely to contribute to the unusually high flexibility of this segment. Two other Gly residues, G33 and G51, which are situated at the termini of the β2 and in the turn between β2 and α3, respectively, also exhibit higher flexibility on average than other residues. These observations are not surprising in light of the greater conformational flexibility of glycine residues due to the lack of side chains. Indeed, statistical analysis of the database of solution NMR-derived backbone order parameters indicates that glycine is the most flexible amino acid.[103]

The high mobility of the N-terminal residues is inferred not only from the lack of signals from D2 and K3 in the spectra but also from the lower order parameter and significantly higher-than-the-average R_1 for I4. Similarly, NMR parameters indicate that R73 are dynamic. In the reassembled thioredoxin, R73 connects to G74 noncovalently through a hydrogen bond, and R73 is situated between the "irregular" 3_{10} helix and the β4 strand. In addition, R73 is on the surface of protein, which is solvent exposed. These factors contribute to the high flexibility of R73.

Besides the mobile residues in turns, loops, and termini, several residues located in the "regular" secondary structure elements, such as T14 and T66, also show higher-than-average mobility. T66, located in a 3_{10} helix, has the lowest order parameter $\langle S \rangle$ among those resolved residues that constitute "regular" secondary structure elements and higher than average R_1. In the X-ray structure, the 3_{10} helix is not well ordered, it is distorted by a 6→1 hydrogen bond between A67(O)−I72(N). The high flexibility of T66 is thus likely related to the distorted 3_{10} structure. T14 is located in middle of α1. In the solution NMR structure, the α1 helix formed by residues S11−K18 is not well-defined. The backbone torsion angles ϕ formed by residues 14−16 are significantly offset from the standard values for helices. In one of the two molecules in the asymmetric unit cell, the α1 helix is highly disordered compared with a regular helical structure, and residues 13−14 exhibit irregular torsion angle (θ, ϕ) values. The unusual dynamics of T14 is probably due to this irregular helical geometry.

Not all residues in turns and loops and at the termini exhibit relatively high flexibility. One such example is T8 and G71. These residues are located in the turn connecting α1 and β1, α3 and β4, respectively. The mobilities of these two residues on the pico- to nanosecond and submicrosecond time scales reflected by R_1 and $\langle S \rangle$ are not higher than the average. The R_1 values of T8 and G71 are 0.023 ± 0.003 and 0.038 ± 0.009 s^{-1}, respectively. Both of these R_1 values are lower than the average. The order parameters for these residues are 0.90 ± 0.03 and 0.93 ± 0.04, respectively, which is higher than the mean value for the protein, indicating more rigid environments.

The two redox-active sites of the protein, C32 and C35, are located at the end of the β3 strand and the beginning of the α4 helix, respectively. In the X-ray structure, the C32 residue is on the surface of the protein and solvent assessable. The high mobility of G33, as shown by solid-state NMR observables, R_1 and $\langle S \rangle$, in current study, suggests its possible functional importance. Similarly, the mobile residue such as R73, which is spatial proximity to the active sites, may also imply its possible functional role in thioredoxin; we note, however, that in reassembled thioredoxin R73 forms the cleavage site, and

(103) Goodman, J. L.; Pagel, M. D.; Stone, M. J. *J. Mol. Biol.* **2000**, *295*, 963–978.

therefore its high mobility may not be functionally significant. Other mobile residues, such as 14 and 19−22 are not related to the catalytic function of thioredoxin, but may play other important roles. However, at present these are not understood and warrant further exploration. As discussed above, the stretch of residues 19−22 is an unusual secondary structure environment, and whether this has any functional implications is not clear. In order to address this question it would be interesting to explore the dynamics of site-directed thioredoxin mutants. We note that unlike the mobile residues above, the highly mobile residues in N-termini may not play any functionally important roles.

It is interesting to compare the solid-state NMR-derived backbone dipolar order parameters measured in different microcrystalline proteins such as GB1, ubiquitin, and reassembled thioredoxin. Even though different sample preparation conditions were followed and different dipolar recoupling methods were employed (T-MREV, LGCP, RN for GB1, ubiquitin and reassembled thioredoxin, respectively), likely leading to systematic differences in dipolar order parameters, the dynamic properties in these proteins are similar. Notably, the three proteins display a variation of dynamics behavior for different secondary structure regions. For example, most of the highly mobile residues reported in these proteins are located in the "irregular" secondary structure elements; these are, for example, G41 in GB1, G47 in ubiquitin, and G21 in reassembled thioredoxin. On other hand, the different mean order parameters observed in these three proteins may likely be due to different internal structure beyond the systematic differences due to the variations in the sample preparation conditions and dipolar recoupling methods.

Relationship between Solid-State NMR Parameters and X-ray B-Factors. The solid-state NMR derived R_1 and $\langle S \rangle$ can be compared to the X-ray B-factors reported previously[76] using Figure 4 as the guide. The B-factors were obtained from the PDB file 2TRX, corresponding to the intact full-length thioredoxin. As an overall tendency, both the solid-state NMR observables (R_1 and $\langle S \rangle$) and the crystallographic B-factors reveal enhanced mobility in the loops, turns, and terminal regions, with R_1 increasing and $\langle S \rangle$ decreasing with the increase of the B-factors (also see Supporting Information, Figure S3). However, there are exceptions. For example, residues with both the highest and the lowest $\langle S \rangle$ exhibit medium B-factors. This discrepancy reflects the different contributions of the individual motional types to the B-factors and the solid-state NMR dynamics parameters. The X-ray B-factor scales with the mean-square fluctuations of the individual atoms around their equilibrium positions and reflects the translational mobility of the individual atoms in the equilibrium state. The relaxation, CSA, and dipolar coupling in solid-state NMR are derived from rotations and librations of the backbone atoms modulating the torsion angles, and these motions could be either cooperative or random on different time scales. In reassembled thioredoxin, we have observed the following exceptions to the overall trend. The B-factors of Y70 and G71 are 23.2 and 22.2 Å^2, respectively, and are significantly higher than the mean level of 16 Å^2. At the same time, these residues are relatively rigid according to the solid-state spin-lattice relaxation, ^{1}H−^{15}N dipolar, and CSA parameters. The R_1 values for these two residues are 0.030 ± 0.009 and 0.046 ± 0.013 s^{-1}, respectively, and are lower than the mean R_1 of 0.055 s^{-1}. The ^{1}H−^{15}N dipolar order parameters are 0.91 ± 0.05 and 0.93 ± 0.04 for Y70 and G71, respectively, both higher than the mean value of 0.89 ± 0.05. δ_σ for G71 is 102 ± 4 ppm, also higher than the average value. In the crystallographic data, the Debye−Waller model relates B-factors to isotropic, independent atomic fluctuations, and the B-factor has contributions from static disorder, from whole-protein rigid-body movement and from internal dynamics, and the model does not distinguish the contributions of these individual components.[104] That Y70 and G71 display high B-factors while the NMR data do not suggest high mobility may be due to static disorder or conformational variability, which would lead to high B-factors without internal dynamics on pico- to millisecond or submillisecond time scales. Another exception is the high B-factor (22.26 Å^2) of G65. G65 shows medium relaxation rate, but it is relatively rigid according to the dipolar order parameter and δ_σ (0.91 ± 0.05 and 108 ± 8 ppm, respectively). Similar to Y70 and G71, this discrepancy may be interpreted as high static disorder or/and conformational variability. The comparison of the X-ray B-factors and dynamics in this study indicates that care should be taken in interpreting the X-ray B-factors in terms of high mobility. High B-factor does not necessarily correlate with high mobility. Static disorder also contributes to the B-factor, even in the absence of dynamics on the NMR time scales.

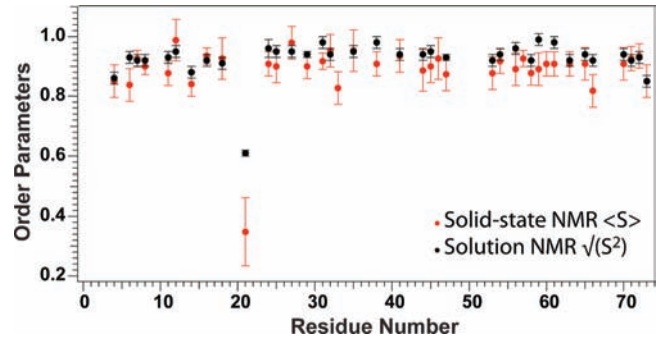

Figure 9. Solid-state dipolar order parameter ⟨S⟩ (red circles) and solution order parameter $(S^2)^{0.5}$ (black circles) plotted as a function of the residue number. Note that order parameters derived from solid-state and solution NMR measurements display similar qualitative trends as a function of the residue number.

Relationship between Solid-State and Solution NMR Parameters. Figure 9 shows the comparison between Lipari−Szabo solution NMR generalized order parameter reported previously[78] and solid-state NMR dipolar order parameter. The dipolar order parameters extracted from solid-state NMR experiments are systematically lower than the generalized order parameters derived from the Lipari−Szabo analysis[105,106] of solution NMR relaxation data, as illustrated in Figure 9. It should be noted that the dipolar order parameters derived from solid-state NMR depend on the rigid limit value of the H−N dipolar coupling constant used as a reference point in the order parameter calculations. For example, if we use N−H dipolar coupling rigid limit value 10.5[107] vs 11.7 kHz,[108] the average order parameters derived from the solid-state NMR measurements presented in this work are 0.96 ± 0.06 vs 0.86 ± 0.06, respectively (while the average solution NMR generalized order parameter $(S^2)^{0.5}$ is 0.93 ± 0.04). So, one should be cautious in interpreting the

(104) Sternberg, M. J. E.; Grace, D. E. P.; Phillips, D. C. *J. Mol. Biol.* **1979**, *130*, 231–252.
(105) Lipari, G.; Szabo, A. *J. Am. Chem. Soc.* **1982**, *104*, 4546–4559.
(106) Lipari, G.; Szabo, A. *J. Am. Chem. Soc.* **1982**, *104*, 4559–4570.
(107) Roberts, J. E.; Harbison, G. S.; Munowitz, M. G.; Herzfeld, J.; Griffin, R. G. *J. Am. Chem. Soc.* **1987**, *109*, 4163–4169.
(108) Cady, S. D.; Hong, M. *J. Magn. Reson.* **2008**, *191*, 219–225.

absolute magnitudes of the solid-state dipolar order parameters in terms of particular motional modes present in the protein. At the same time, comparison of the overall trends in the solid-state dipolar and solution generalized order parameters reveals flexibility in the same regions of the protein. For example, residues I4, T14, and A19−G21 exhibit order parameters significantly lower than the mean values according to both solid-state and solution NMR results. There is one notable exception: N59, which has the highest solution order parameter and medium dipolar solid-state NMR order parameter, indicating that N59 is rigid in solution but undergoes motion in the solid state. The solid-state R_1 value of N59 is also medium range. This discrepancy between solution and solid-state results is possibly related to the different sample state.

Conclusions

We have presented a dynamics study on multiple time scales in the reassembled 1−73(U-^{13}C,^{15}N)/74−108(U-^{15}N) thioredoxin prepared as hydrated precipitate, using a combination of spin-lattice relaxation rate, dipolar order parameter, and anisotropic line shape analyses, as well as signal intensity analysis from variable-temperature and ^{1}H T_2'-filtered NCA measurements. The complete resonance assignments in reassembled thioredoxin available from the pervious studies enable site-specific dynamics analysis using a series of 2D and 3D MAS NMR experiments. The solid-state NMR longitudinal relaxation rates R_1 were observed in the range from 0.012 to 0.64 s^{-1}, in contrast with the much smaller variations observed in the corresponding solution NMR R_1. Site-specific ^{1}H−^{15}N dipolar line shapes extracted from the 3D DIPSHIFT experiment indicate generally high variation of backbone mobility of individual residues in the hydrated PEG-precipitated thioredoxin, with the ^{1}H−^{15}N dipolar order parameter spanning the range from 0.35 ± 0.11 to 0.99 ± 0.07. The chemical shift anisotropy parameters derived from 3D ROCSA measurements show dynamics trends similar to those observed in the ^{1}H−^{15}N dipolar order parameters. The analysis of the dynamics parameters derived from solid-state NMR reveals higher mobility in the residues belonging to the "irregular" secondary structure elements, such as turns, loops, and termini, compared to those constituting the α-helices and β-sheets. The solid-state and solution NMR order parameters display similar qualitative trends as a function of the residue number. The comparison of the solid-state NMR derived dynamics parameters to the X-ray B-factors reveals static disorder contributions to the B-factors. The results of this study bring new insight on the correlation between motions on the different time scales and show the potential of multiple complementary measurements to yield the most detailed picture of the motions present in the solid proteins.

Acknowledgment. The authors thank Marcela Cataldi and Dabeiba Marulanda for the preparation of the thioredoxin samples and Sivakumar Paramasivam for the discussion of the ROCSA and DIPSHIFT experiments. The authors are very grateful to Alexander J. Vega for reading the manuscript and for many insightful suggestions. This project was supported by the National Institutes of Health (NIH Grant Number P20 RR-015588 from the National Center for Research Resources). M.L.T. is supported by the National Science Foundation (MCB-0517592) award and the National Institutes of Health (NIH Grant Number 5G12RR03060 from the National Center for Research Resources) grant to the 600 MHz NMR spectrometer at CCNY. M.L.T. is a member of the New York Structural Biology Center (NYSBC) supported by the National Institutes of Health (GM66354).

Supporting Information Available: Tables with solid-state NMR dynamics parameters of 1−73(U-^{13}C,^{15}N)/74−108(U-^{15}N) reassembled thioredoxin and rmsd of ^{15}N CSA simulations; figures displaying (1) the pulse sequence for the ^{1}H T_2'-edited ^{15}N CP experiment and the ^{1}H T_2' ^{15}N CP spectrum of assembled thioredoxin, (2) the absolute intensities in the 2D NCA spectrum of 1−73(U-^{13}C,^{15}N)/74−108(U-^{15}N) reassembled thioredoxin at 238 K (−35 °C) plotted against the dynamics parameters derived from the solid-state NMR experiments, R_1 and $\langle S \rangle$, (3) X-ray B-factor against solid state NMR dynamics parameters, (4) ^{15}N CSA line shape simulations, and (5) uncertainty estimates in the ^{15}N CSA simulations. This material is available free of charge via the Internet at http://pubs.acs.org.

JA9037802